# ON THE SOLUTION OF THE COMPRESSIBLE FLOW EQUATIONS AT SMALL MACH NUMBERS

**Renan de S. Teixeira, renannovoser@gmail.com**
**Leonardo S. de B. Alves, leonardo_alves@ime.eb.br**
Departamento de Engenharia Mecânica e de Materiais, Instituto Militar de Engenharia, Rio de Janeiro, Brazil.

**Ann R. Karagozian, ark@seas.ucla.edu**
**Robert E. Kelly, rekhome@ucla.edu**
Department of Mechanical and Aerospace Engineering, University of California at Los Angeles, Los Angeles, USA.

***Abstract.*** *The present paper focuses on the development of a code capable of performing numerical simulations of transient flows at all speeds. For this purpose, we employ an algorithm based on the dual-time preconditioning of the compressible flow equations developed by the aerospace research community throughout the past two decades. Using this procedure, the fluid mechanics and heat transfer phenomena associated not only with compressible flows but also with incompressible flows as well can be simulated using a single robust algorithm. In order to demonstrate such characteristics, classical one-, two- and three-dimensional incompressible problems are solved with this algorithm, namely: Couette and Poiseuille flows (1D), planar mixing-layer (2D), and free jet (3D). These results were obtained with a code prepared under a Finite-Difference framework using a non-uniform Cartesian grid, second-order standard central differencing with a fourth-order preconditioned artificial dissipation, second-order implicit physical-time marching and implicit Euler pseudo-time marching with approximate factorization.*

***Keywords:*** *Compressible Flow, Small Mach Number, Dual-Time Preconditioning*

## 1. INTRODUCTION

Numerical methods in transport phenomena are considered robust when applicable to compressible and incompressible flows efficiently. In a continuous sense, the compressible set of equations approaches the incompressible one when the Mach number approaches zero, i.e., $M \rightarrow 0$ (Klainerman and Majda, 1982). However, when solving these equations numerically one has to use their discrete form. This leads to a significant problem: Density becomes pressure independent in the limit of low Mach numbers, leading to the amplification of pressure round-off errors in standard algorithms when $M < 0.3$ (Sesterhenn et al., 1999). This affects not only convergence but also accuracy, and leads to significant differences between pressure fluctuations obtained from continuous and discrete sets of equations (Guillard and Viozat, 1999).

Two different approaches can be taken when developing numerical methods that are capable of solving problems in transport phenomena at all speeds. Traditionally, these approaches have been referred to as pressure-based methods and density-based methods. In order to avoid possible misinterpretation, these approaches are now defined:
**Pressure-Based Methods:** Pressure is obtained from a new equation derived by combining at least two of the three (mass, momentum and energy) conservation equations. The equation of state can then be used to solve for either density or temperature. Hence, the system becomes over-determined and one of the conservation equations is dropped.
**Density-Based Methods:** The original conservation equations are kept. However, a dependent variable Jacobian is introduced to allow pressure, as well as temperature or entropy, to be solved for directly. This Jacobian is properly modified so that convective and acoustic speeds are of the same order. Density is obtained from the equation of state.

Pressure-based methods were born out of the heat transfer community in an attempt to extend codes primarily designed for incompressible flows towards compressible flow regimes. Incompressible flow codes have traditionally used a Poisson equation for pressure, which is efficiently solved for by employing multigrid acceleration procedures. However, the strong conservation form of the governing equations is not strictly satisfied. As a direct consequence, these methods have not yet been widely utilized by the aerospace community.

On the other hand, density-based methods were born out of the aerospace community in an attempt to extend codes primarily designed for compressible flows towards incompressible flow regimes. The modified Jacobian or preconditioning acts on a pseudo-time scale that vanishes once converged, either within each physical-time step or towards steady-state. Hence, the original conservation equations are always recovered. However, preconditioning methods force the system of equations to be either parabolic or hyperbolic. Hence, they are not as efficient as pressure-based methods due to the fact that multigrid acceleration procedures are far more efficient when applied to elliptic systems of equations.

The density-based approach developed by Merkle and co-workers (Venkateswaran and Merkle, 2000; Buelow et al., 2001) known as dual-time preconditioning is employed in the present paper. The code was developed under a Finite-Difference framework using a non-uniform Cartesian grid, second-order standard central differencing with a fourth-order preconditioned artificial dissipation, second-order implicit physical-time marching and implicit Euler pseudo-time marching with approximate factorization. The incompressible Couette and Poiseuille flows, planar mixing-layer, and free and transverse jets are used as test cases.

## 2. GOVERNING EQUATIONS

The time-accurate three-dimensional preconditioned governing equations are given by

$$\mathbf{\Gamma}\,\frac{\partial \hat{\mathbf{Q}}}{\partial \tau}+\frac{\partial \mathbf{Q}}{\partial t}+\frac{\partial}{\partial x}\left(\mathbf{E}_i-\mathbf{E}_v\right)+\frac{\partial}{\partial y}\left(\mathbf{F}_i-\mathbf{F}_v\right)+\frac{\partial}{\partial z}\left(\mathbf{G}_i-\mathbf{G}_v\right)=\mathbf{H}\,, \tag{1}$$

where the old and new set of variables $\mathbf{Q}$ and $\hat{\mathbf{Q}}$ are given by

$$\mathbf{Q}=\left(\rho,\rho\,u,\rho\,v,\rho\,w,\rho\,E,\rho\,Y_1,\,\ldots,\rho\,Y_{N-1}\right)^T \quad \text{and} \quad \hat{\mathbf{Q}}=\left(\,p_g,u,v,w,T,Y_1,...,Y_{N-1}\,\right)^T\,, \tag{2}$$

with $\rho$ standing for density, $p=p_0+p_g$ for pressure, with $p_0$ standing for the constant reference (atmospheric) pressure and $p_g$ for the gage pressure, $u$, $v$ and $w$ for the Cartesian velocity components, $e$ for thermal internal energy, $E=e+\left(u^2+v^2+w^2\right)/2$ for total internal energy, $Y_i$ for mass fraction of species $i$ and $N$ for the total number of species in the mixture. The inviscid and viscous fluxes $\mathbf{E_i}$, $\mathbf{F_i}$, $\mathbf{G_i}$, $\mathbf{E_v}$, $\mathbf{F_v}$ and $\mathbf{G_v}$ have a standard definition and $\mathbf{H}$ represents the source term, which is zero in the current work.

In conventional compressible flow numerical algorithms, temperature and pressure are calculated iteratively from the equations (Shuen et al., 1992; 1993),

$$e=h-\frac{p}{\rho}\quad,\quad h=\sum_{i=1}^{N}Y_i\,h_i\quad,\quad h_i=h_{f,i}^{o}+\int_{T_{ref}}^{T}c_{p,i}\,dT\quad\text{and}\quad p=\rho\,\bar{R}\,T\sum_{i=1}^{N}\frac{Y_i}{W_i}\,, \tag{3}$$

with $h$ representing the enthalpy per unit mass and $T_{ref}$ the reference temperature for thermodynamic properties. The properties of the species $i$ are the molecular weight $W_i$, the constant pressure specific heat $c_{p,i}$, the thermodynamic enthalpy per unit mass $h_i$ and the heat of formation per unit mass $h_{f,i}^{o}$. Although only thermally perfect gases were considered, the code was written in such a way to allow for arbitrary equations of state (Merkle et al., 1998).

The preconditioning matrix $\mathbf{\Gamma}$ is given by

$$\mathbf{\Gamma}=\begin{pmatrix}
\rho_P & 0 & 0 & 0 & \rho_T & \rho_{Y_1} & \cdots & \rho_{Y_{N-1}} \\
u\,\rho_P & \rho & 0 & 0 & u\,\rho_T & u\,\rho_{Y_1} & \cdots & u\,\rho_{Y_{N-1}} \\
v\,\rho_P & 0 & \rho & 0 & v\,\rho_T & v\,\rho_{Y_1} & \cdots & v\,\rho_{Y_{N-1}} \\
w\,\rho_P & 0 & 0 & \rho & w\,\rho_T & v\,\rho_{Y_1} & \cdots & w\,\rho_{Y_{N-1}} \\
H\rho_P-\left(1-\frac{\partial h}{\partial P}\right) & \rho\,u & \rho\,v & \rho\,w & H\rho_T+\rho\frac{\partial h}{\partial T} & H\rho_{Y_1}+\rho\frac{\partial h}{\partial Y_1} & \cdots & H\rho_{Y_{N-1}}+\rho\frac{\partial h}{\partial Y_{N-1}} \\
Y_1\,\rho_P & 0 & 0 & 0 & Y_1\,\rho_T & \rho+Y_1\,\rho_{Y_1} & \cdots & Y_1\,\rho_{Y_{N-1}} \\
\vdots & \vdots & \vdots & \vdots & \vdots & \vdots & \ddots & \vdots \\
Y_{N-1}\,\rho_P & 0 & 0 & 0 & Y_{N-1}\,\rho_T & Y_{N-1}\,\rho_{Y_1} & \cdots & \rho+Y_{N-1}\,\rho_{Y_{N-1}}
\end{pmatrix}, \tag{4}$$

with the total enthalpy of the gas mixture being $H=h+\left(u^2+v^2+w^2\right)/2$. For our preconditioning matrix we define

$$\rho_P=\frac{1}{V_p^2}-\rho_T\left(1-\rho\,\frac{\partial h}{\partial P}\right)\Bigg/\left(\rho\,\frac{\partial h}{\partial T}\right)\quad,\quad \rho_T=\delta\,\frac{\partial \rho}{\partial T}\quad\text{and}\quad \rho_{Y_i}=\delta\,\frac{\partial \rho}{\partial Y_i}\quad, \tag{5}$$

where $V_p$ is the preconditioning velocity. Setting $\delta=0$ selects Shuen et al. (1993)'s preconditioning and setting $\delta=1$ selects Choi and Merkle (1993)'s preconditioning.

The inviscid modes of the dual-time preconditioned system of equations (1) are obtained from the eigenvalues of $\mathbf{\Gamma}^{-1}\hat{\mathbf{A}}$, $\mathbf{\Gamma}^{-1}\hat{\mathbf{B}}$ and $\mathbf{\Gamma}^{-1}\hat{\mathbf{C}}$, where $\hat{\mathbf{A}}=\partial\mathbf{E}_i/\partial\hat{\mathbf{Q}}$, $\hat{\mathbf{B}}=\partial\mathbf{F}_i/\partial\hat{\mathbf{Q}}$ and $\hat{\mathbf{C}}=\partial\mathbf{G}_i/\partial\hat{\mathbf{Q}}$. These Jacobians are given by

$$\hat{\mathbf{A}}=\begin{pmatrix}
u\,\frac{\partial\rho}{\partial P} & \rho & 0 & 0 & u\,\frac{\partial\rho}{\partial T} & u\,\frac{\partial\rho}{\partial Y_1} & \cdots & u\,\frac{\partial\rho}{\partial Y_{N-1}} \\
1+u^2\,\frac{\partial\rho}{\partial P} & 2\,\rho\,u & 0 & 0 & u^2\,\frac{\partial\rho}{\partial T} & u^2\,\frac{\partial\rho}{\partial Y_1} & \cdots & u^2\,\frac{\partial\rho}{\partial Y_{N-1}} \\
u\,v\,\frac{\partial\rho}{\partial P} & \rho\,v & \rho\,u & 0 & u\,v\,\frac{\partial\rho}{\partial T} & u\,v\,\frac{\partial\rho}{\partial Y_1} & \cdots & u\,v\,\frac{\partial\rho}{\partial Y_{N-1}} \\
u\,w\,\frac{\partial\rho}{\partial P} & \rho\,w & 0 & \rho\,u & u\,w\,\frac{\partial\rho}{\partial T} & u\,w\,\frac{\partial\rho}{\partial Y_1} & \cdots & u\,w\,\frac{\partial\rho}{\partial Y_{N-1}} \\
u\,\frac{\partial(\rho H)}{\partial P} & \rho\left(H+u^2\right) & \rho\,u\,v & \rho\,u\,w & u\,\frac{\partial(\rho H)}{\partial T} & u\,\frac{\partial(\rho H)}{\partial Y_1} & \cdots & u\,\frac{\partial(\rho H)}{\partial Y_{N-1}} \\
u\,Y_1\,\frac{\partial\rho}{\partial P} & \rho\,Y_1 & 0 & 0 & u\,Y_1\,\frac{\partial\rho}{\partial T} & u\,\frac{\partial(\rho Y_1)}{\partial Y_1} & \cdots & u\,\frac{\partial(\rho Y_1)}{\partial Y_{N-1}} \\
\vdots & \vdots & \vdots & \vdots & \vdots & \vdots & \ddots & \vdots \\
u\,Y_{N-1}\,\frac{\partial\rho}{\partial P} & \rho\,Y_{N-1} & 0 & 0 & u\,Y_{N-1}\,\frac{\partial\rho}{\partial T} & u\,\frac{\partial(\rho Y_{N-1})}{\partial Y_1} & \cdots & u\,\frac{\partial(\rho Y_{N-1})}{\partial Y_{N-1}}
\end{pmatrix}, \tag{6}$$

$$\hat{\mathbf{B}}=\begin{pmatrix} v\,\frac{\partial\rho}{\partial P} & 0 & \rho & 0 & v\,\frac{\partial\rho}{\partial T} & v\,\frac{\partial\rho}{\partial Y_1} & \cdots & v\,\frac{\partial\rho}{\partial Y_{N-1}} \\ u\,v\,\frac{\partial\rho}{\partial P} & \rho\,v & \rho\,u & 0 & u\,v\,\frac{\partial\rho}{\partial T} & u\,v\,\frac{\partial\rho}{\partial Y_1} & \cdots & u\,v\,\frac{\partial\rho}{\partial Y_{N-1}} \\ 1+v^2\,\frac{\partial\rho}{\partial P} & 0 & 2\,\rho\,v & 0 & v^2\,\frac{\partial\rho}{\partial T} & v^2\,\frac{\partial\rho}{\partial Y_1} & \cdots & v^2\,\frac{\partial\rho}{\partial Y_{N-1}} \\ v\,w\,\frac{\partial\rho}{\partial P} & 0 & \rho\,w & \rho\,v & v\,w\,\frac{\partial\rho}{\partial T} & v\,w\,\frac{\partial\rho}{\partial Y_1} & \cdots & v\,w\,\frac{\partial\rho}{\partial Y_{N-1}} \\ v\,\frac{\partial(\rho H)}{\partial P} & \rho\,u\,v & \rho\left(H+v^2\right) & \rho\,v\,w & v\,\frac{\partial(\rho H)}{\partial T} & v\,\frac{\partial(\rho H)}{\partial Y_1} & \cdots & v\,\frac{\partial(\rho H)}{\partial Y_{N-1}} \\ v\,Y_1\,\frac{\partial\rho}{\partial P} & 0 & \rho\,Y_1 & 0 & v\,Y_1\,\frac{\partial\rho}{\partial T} & v\,\frac{\partial(\rho Y_1)}{\partial Y_1} & \cdots & v\,\frac{\partial(\rho Y_1)}{\partial Y_{N-1}} \\ \vdots & \vdots & \vdots & \vdots & \vdots & \vdots & \ddots & \vdots \\ v\,Y_{N-1}\,\frac{\partial\rho}{\partial P} & 0 & \rho\,Y_{N-1} & 0 & v\,Y_{N-1}\,\frac{\partial\rho}{\partial T} & v\,\frac{\partial(\rho Y_{N-1})}{\partial Y_1} & \cdots & v\,\frac{\partial(\rho Y_{N-1})}{\partial Y_{N-1}} \end{pmatrix}, \tag{7}$$

$$\hat{\mathbf{C}}=\begin{pmatrix} w\,\frac{\partial\rho}{\partial P} & 0 & 0 & \rho & w\,\frac{\partial\rho}{\partial T} & w\,\frac{\partial\rho}{\partial Y_1} & \cdots & w\,\frac{\partial\rho}{\partial Y_{N-1}} \\ u\,w\,\frac{\partial\rho}{\partial P} & \rho\,w & 0 & \rho\,u & u\,w\,\frac{\partial\rho}{\partial T} & u\,w\,\frac{\partial\rho}{\partial Y_1} & \cdots & u\,w\,\frac{\partial\rho}{\partial Y_{N-1}} \\ v\,w\,\frac{\partial\rho}{\partial P} & 0 & \rho\,w & \rho\,v & v\,w\,\frac{\partial\rho}{\partial T} & v\,w\,\frac{\partial\rho}{\partial Y_1} & \cdots & v\,w\,\frac{\partial\rho}{\partial Y_{N-1}} \\ 1+w^2\,\frac{\partial\rho}{\partial P} & 0 & 0 & 2\,\rho\,w & w^2\,\frac{\partial\rho}{\partial T} & w^2\,\frac{\partial\rho}{\partial Y_1} & \cdots & w^2\,\frac{\partial\rho}{\partial Y_{N-1}} \\ w\,\frac{\partial(\rho H)}{\partial P} & \rho\,u\,w & \rho\,v\,w & \rho\left(H+w^2\right) & w\,\frac{\partial(\rho H)}{\partial T} & w\,\frac{\partial(\rho H)}{\partial Y_1} & \cdots & w\,\frac{\partial(\rho H)}{\partial Y_{N-1}} \\ w\,Y_1\,\frac{\partial\rho}{\partial P} & 0 & 0 & \rho\,Y_1 & w\,Y_1\,\frac{\partial\rho}{\partial T} & w\,\frac{\partial(\rho Y_1)}{\partial Y_1} & \cdots & w\,\frac{\partial(\rho Y_1)}{\partial Y_{N-1}} \\ \vdots & \vdots & \vdots & \vdots & \vdots & \vdots & \ddots & \vdots \\ w\,Y_{N-1}\,\frac{\partial\rho}{\partial P} & 0 & 0 & \rho\,Y_{N-1} & w\,Y_{N-1}\,\frac{\partial\rho}{\partial T} & w\,\frac{\partial(\rho Y_{N-1})}{\partial Y_1} & \cdots & w\,\frac{\partial(\rho Y_{N-1})}{\partial Y_{N-1}} \end{pmatrix}, \tag{8}$$

where we have

$$\frac{\partial(\rho H)}{\partial P}=H\frac{\partial\rho}{\partial P}+\rho\frac{\partial h}{\partial P}\ ,\ \frac{\partial(\rho H)}{\partial T}=H\frac{\partial\rho}{\partial T}+\rho\frac{\partial h}{\partial T}\ ,\ \frac{\partial(\rho H)}{\partial Y_i}=H\frac{\partial\rho}{\partial Y_i}+\rho\frac{\partial h}{\partial Y_i}\ ,$$

$$\frac{\partial(\rho Y_i)}{\partial Y_i}=\rho+Y_i\frac{\partial\rho}{\partial Y_i}\quad\text{and}\quad\frac{\partial(\rho Y_i)}{\partial Y_j}=Y_i\frac{\partial\rho}{\partial Y_j}\ . \tag{9}$$

The preconditioning matrix $\mathbf{\Gamma}$ does not affect the eigenvalues associated with the particle wave speeds. However, this matrix acts through the preconditioning velocity $V_p$ in relations (5) to modify the speed of sound in such a way that the particle and acoustic wave speeds have the same order of magnitude. The acoustic wave speeds of the inviscid Jacobian $\mathbf{A}$ is then transformed into the pseudo-acoustic wave speeds

$$u\pm c\rightarrow\frac{u}{2}\left(1+\frac{V_p^2}{c^2}\right)\pm\sqrt{V_p^2+\left\{\frac{u}{2}\left(1-\frac{V_p^2}{c^2}\right)\right\}^2}\ , \tag{10}$$

of the preconditioned inviscid Jacobians $\mathbf{\Gamma}^{-1}\hat{\mathbf{A}}$. The same is true for the eigenvalues of $\mathbf{B}$ and $\mathbf{C}$, which are respectively related to $\mathbf{\Gamma}^{-1}\hat{\mathbf{B}}$ and $\mathbf{\Gamma}^{-1}\hat{\mathbf{C}}$.The speed of sound $c$ is given by relation

$$\frac{\partial\rho}{\partial P}=\frac{1}{c^2}-\frac{\partial\rho}{\partial T}\left(1-\rho\,\frac{\partial h}{\partial P}\right)\Bigg/\left(\rho\,\frac{\partial h}{\partial T}\right)\ , \tag{11}$$

which is written this way for purposes of comparison with equation (5).

Because we will consider thermally perfect gases only in this work, we have

$$\frac{\partial\rho}{\partial P}=\frac{1}{RT}\ ,\ \frac{\partial\rho}{\partial T}=-\frac{\rho}{T}\ ,\ \frac{\partial\rho}{\partial Y_i}=-\rho\frac{(R_i-R_N)}{R}\ ,\ \frac{\partial h}{\partial P}=0\ ,\ \frac{\partial h}{\partial T}=c_p\ \text{ and }\ \frac{\partial h}{\partial Y_i}=h_i-h_N\ . \tag{12}$$

## 3. RESULTS AND DISCUSSION

The dual-time step integration procedure used in this study works in the following way. At each physical-time step, we iterate the discretized version of equation (1) with an implicit Euler discretization in pseudo-time until the pseudo-time derivative $\partial\hat{\mathbf{Q}}/\partial\tau$ becomes as close to zero as one arbitrarily specifies ($error=\epsilon$). At this point, equation (1) will be similar up to $O(\epsilon)$ to the un-preconditioned equation. If one then desires a time accurate solution, $\epsilon$ can be set to be very small at each physical-time step. Otherwise, if one only desires a steady-state solution, only a couple of orders of magnitude of convergence in pseudo-time are needed during the initial physical transient, i.e., $\epsilon$ can be relatively large. As the solution approaches the physical steady-state, $\epsilon$ is then set to be very small. The pseudo-time step $\Delta\tau$ is thus chosen for optimum convergence of the iteration procedure, whereas the physical-time step $\Delta t$ is chosen, in theory, according to the physics that one wants to resolve. In practice however, $\Delta t$ is constrained by the sensitivity of the preconditioned scheme to initial conditions and to nonlinear gradients (Venkateswaran and Merkle, 2000).

The code used was prepared under a Finite-Difference framework using a non-uniform Cartesian grid, with a second order standard central differencing together with a fourth order artificial dissipation, and a second order physical-time backwards discretization. A first order implicit pseudo-time marching was employed, which was solved using an alternating direction approach to approximately factor the implicit matrix, yielding three block tri-diagonal matrix systems solved in separate steps (Tannehill et al., 1997). Further details about the code developed and the test cases shown next are given by Alves (2006).

### 3.1 One-Dimensional Flows

One of the problems we tackled here is known as the transient planar Couette flow. This simple shear flow shows how a fluid, which we chose to be air at ambient temperature and pressure, that is trapped in between two parallel plates behaves when the upper plate suddenly starts to move at a constant speed. We chose the Mach number and the Reynolds number of the upper plate to be $M = 10^{-3}$ and $Re = 2152.5$, where the upper plate axial velocity is $U_W$ and the distance between plates is $L$. Hence, we are simulating an essentially incompressible, viscous flow yet with a compressible scheme. The transient evolution of this flow was obtained using our implicit code and is shown in Figure 1 (left). The axial velocity in this problem moves from its initial profile towards its well known linear steady-state profile. In this figure, the physical-time between two consecutive curves is constant and equal to $25\,\Delta t_0$, where $\Delta t_0$ was chosen close to the maximum physical-time step allowed by the scheme for the first physical-time iteration. The data points shown were obtained from a separation of variables solution derived for purposes of comparison. Good agreement between both solutions exists for all physical-time steps.

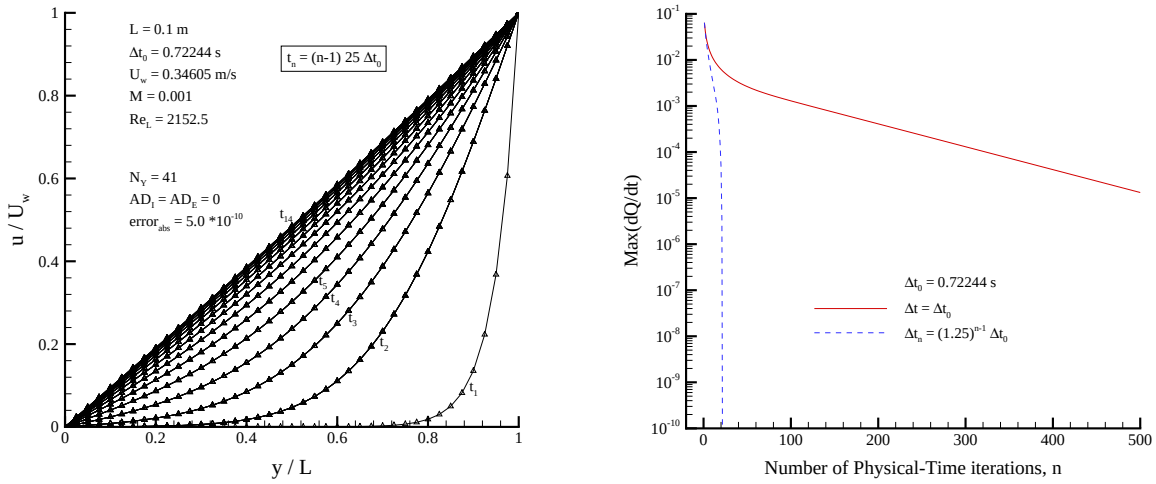


Figure 1. (left) Transient Couette flow simulation with $M = 10^{-3}$. Data points obtained from separation of variables solution. (right) Steady-State convergence acceleration of Couette flow problem using a variable physical-time step.

Different ways of accelerating convergence towards steady-state are shown in Figure 1 (right). This figure shows the maximum in the magnitude of the physical-time derivative vector $Max(\partial \mathbf{Q}/\partial t)$ as the physical-time iterations are performed. The solid line shows the convergence towards steady-state of the case shown in Figure 1 (left), where a constant physical-time step $\Delta t_0$ was used. The blue dashed line shows the convergence towards steady-state of the same case, but with a physical-time step that increases in time according to $\Delta t_n = (1.25)^{n-1}\,\Delta t_0$, where $n$ is the physical-time iteration number. In both cases, the pseudo-time iterations were performed until the maximum absolute error of the residue's $L_2$ norm was below $\epsilon = 5 \times 10^{-10}$, which is close to machine precision for this particular problem. The average number of pseudo-time iterations per physical-time iteration was about one order of magnitude higher for the $\Delta t_n$ case than for the $\Delta t_0$ case. However, the number of physical-time iterations needed for convergence towards steady-state in the $\Delta t_n$ case was several orders of magnitude lower than in the $\Delta t_0$ case. Hence, the computational time required for driving the solution towards steady-state was greatly reduced when a variable physical-time step was used.

In order to reduce the computational cost when converging a solution towards steady-state, one could also relax the precision requirements imposed to the residue during the transient process. Only a couple of orders of magnitude in residue reduction are needed when iterating in pseudo-time during the physical transient. Once the solution approaches the specified steady-state, the precision requirements in terms of orders of magnitude in residue reduction could be slowly increased. This way, the minimum number of pseudo-time iterations is performed per physical-time step.

The other classical viscous flow problem we looked at is the planar Poiseuille Flow, which is a pressure gradient driven flow of a fluid in between parallel plates. Once again the fluid is chosen to be air at ambient temperature and pressure. The pressure gradient imposed generates an essentially incompressible flow with $M = 2.32 \times 10^{-4}$ and $Re_L = 500$, based on the maximum steady-state velocity $U_{max}$ and the distance between plates $L$. The transient evolution of this flow field obtained by our implicit code is shown in Figure 2 (left), where one can see the solution moving towards the well known parabolic steady-state velocity profile. The time increment between consecutive curves is equal to the physical-time step used and is given by $\Delta t_0$. The pseudo-time iterations were performed until the transient residue was below an arbitrarily specified value ($\epsilon = 10^{-8}$). The data points shown were obtained from a separation of variables solution derived for purposes of comparison. Although both steady-state solutions agree down to machine precision, there is a small deviation at the initial time steps. The reason for this lack of agreement is the fact that the pressure gradient within the computational domain is allowed to vary in time during the numerical simulation, but the separation of variables solution was derived considering such pressure gradient constant.

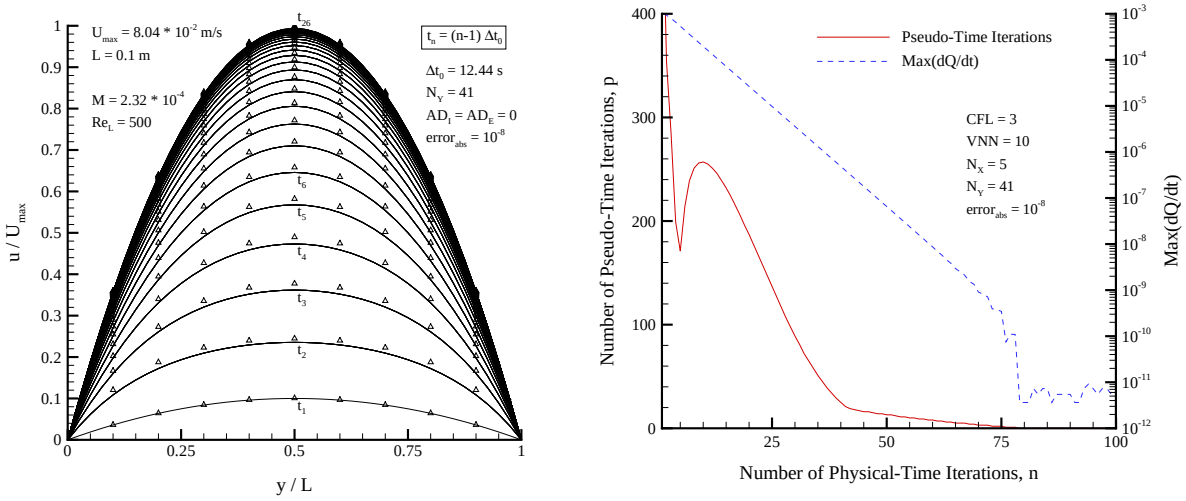


Figure 2. (left) Transient Poiseuille flow simulation with $M = 2.32 \times 10^{-4}$. Data points obtained from separation of variables solution. (right) Pseudo-time iterations and maximum physical-time derivative of the transient Poiseuille flow problem as functions of physical-time iterations.

Convergence to steady-state can also be seen in Figure 2 (right), which shows the number of pseudo-time iterations and the maximum physical-time derivative as functions of the number of physical-time iterations. As we can see, the number of pseudo-time iterations decreases to 1 as the flow field approaches steady-state, which is reached in about 75 physical-time iterations.

### 3.2 Two-Dimensional Flows

The next test case studied is known as the planar mixing layer. This flow is formed when two streams with different speeds meet downstream of a splitter plate. Here, the maximum streamwise velocity of lower stream is given by $U_1$, whereas the maximum streamwise velocity of the upper stream is given by $U_2$, which is less than $U_1$. The splitter plate is not present in our simulation. The inlet conditions for the velocity profile at the initiation of the shear layer were either the self-similar boundary layer profile or the hyperbolic tangent profile, both with a pre-specified vorticity or momentum thickness. The self-similar solution was obtained by solving the well known Blasius equation with a modified finite difference code developed to solve the general Falkner-Skan self-similar equations (Wilcox, 2000).

All variables but pressure, which was extrapolated ($\partial p/\partial x = 0$), were specified at the inlet boundary. At the exit boundaries, only the pressure was prescribed whereas the other variables were extrapolated ($\partial/\partial x = 0$). Two different cross-stream boundary conditions for the streamwise velocity were simulated, namely $u = U_1$ or $U_2$ and $\partial u/\partial y = 0$. No major differences between these two cases were found, and the latter condition was used.

As it is well known, this flow is unstable to inviscid disturbances of certain frequencies. Hence, in order to compare our solution to the classical steady-state self-similar one, the Reynolds number and the domain size had to be small enough so that random disturbances would not be amplified within the chosen domain. Figure 3 (left) shows the spatial development of the steady-state mixing layer with $M_1 = 10^{-4}$ ($Re_{1,\delta_0} = 9.82$) and $U_2/U_1 = 0.5$ obtained by our implicit code with $CFL = 3$ and $VNN = 10$. Once again air at ambient pressure and temperature was considered. The cross-stream coordinate is made dimensionless using the local vorticity thickness ($\delta_v = (U_2 - U_1)/(\partial u/\partial y)_{y=0}$), which shows that the flow is indeed self-similar. For the sake of comparison, the inlet self-similar solution is also shown. The small discrepancies present are due to oscillations introduced by the central-differencing used.

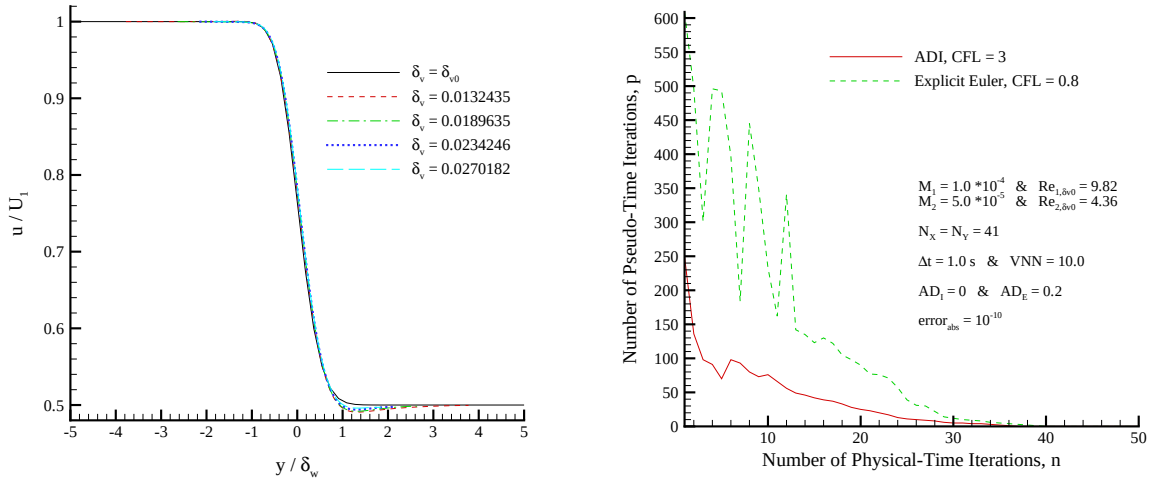


Figure 3. (left) Streamwise velocity profiles normalized with respect to the local vorticity thickness. (right) Pseudo-time iterations as functions of physical-time iterations for explicit Euler and ADI schemes with $\Delta x/\Delta y = 1$.

The number of pseudo-time iterations per physical-time iteration are shown in Figure 3 (right) for both the explicit Euler ($CFL = 0.8$) and ADI ($CFL = 3$) schemes used. One can see in this figure that the implicit scheme needs fewer pseudo-time iterations to converge than does the explicit scheme. The explicit Euler method suffers the most when the grid aspect ratio differs from one ($\Delta x/\Delta y = 1$ in the present case). In such non-unity aspect ratio cases, the advantages one obtains by using the ADI scheme over the explicit Euler one become even greater.

Figure 4 shows the behavior of our ADI scheme for different computational control parameters ($CFL$ and $VNN$) when the grid aspect ratio is and the Reynolds number is 10 times larger than the one used in the previous investigation ($M_1 = 10^{-3}$ and $Re_{1,\theta_0} = 67.87$). The inlet condition used here was imposed using a hyperbolic tangent profile. The Reynolds numbers reported here are based on the inlet momentum thickness ($\theta_0 = 0.3165\, mm$). Figure 4 (left) shows the convergence of the gage pressure pseudo-time increment $\Delta p_g$ for the first physical-time iteration with $VNN = 10$ and several different $CFL$ numbers. We can observe in this figure that the optimum $CFL$ number is close to $CFL = 3$, which is within the known optimum range for the ADI scheme. Figure 4 (right) shows the pseudo-time convergence of the gage pressure for the first physical-time iteration again for the same set of parameters, but now with $CFL = 3$ and several different $VNN$ values. We can see in this figure the concept of maximum $VNN$. As this parameter is increased, convergence improves until an optimum convergence is achieved. Beyond this value of $VNN = 0.5$, no improvement in convergence is observed.

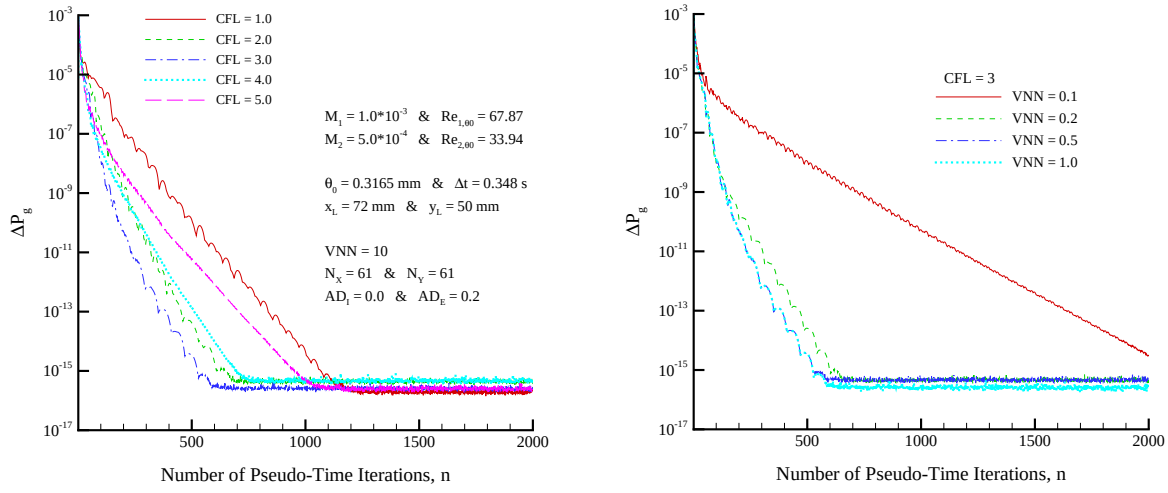


Figure 4. Gage pressure pseudo-time convergence with $\Delta x/\Delta y \simeq 1.44$ for (left) $VNN = 10$ and several different $CFL$ numbers and (right) $CFL = 3$ and several different $VNN$.

The linear and nonlinear evolution of the unstable planar mixing layer is also investigated. Low amplitude forcing of disturbances were used to perturb this flow field. These disturbances, with selected frequencies $\omega$ ($= 2\,\pi\,f^*\,\theta_0/U_1$), were obtained from the classical linear stability analysis for the planar mixing layer problem using a hyperbolic tangent profile. They were superposed with a $2\%$ amplitude to an inlet profile with maximum inlet Reynolds numbers equal to $Re_{1,\theta_0} = 67.87$ and $Re_{2,\theta_0} = 33.94$ ($U_2/U_1 = 0.5$), and an inlet momentum thickness equal to $\theta_0 = 0.3165\,mm$. The domain size and time span used in the numerical computations were based on the linear stability disturbance wavelength $\Lambda_{LSA}$ and period $T_{LSA}$. Grid resolution studies were performed beforehand to ensure converged results.

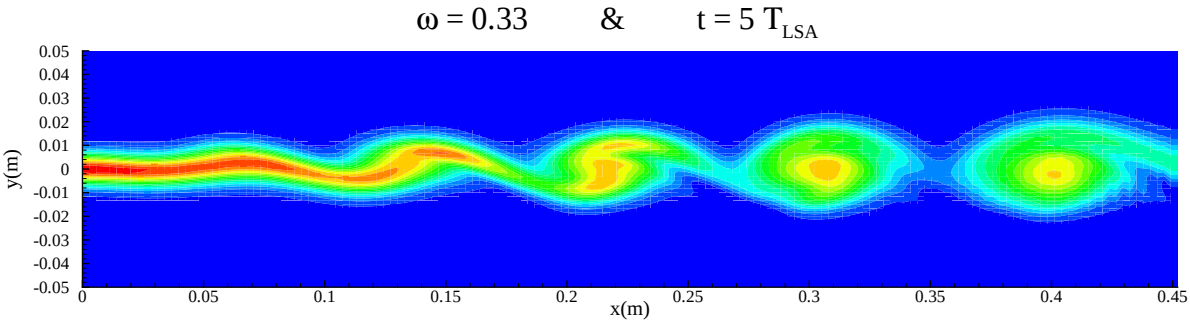


Figure 5. Vorticity contour plot for the $\omega = 0.33$ case at $t = 5\,\mathcal{T}_{LSA}$. The numerically simulated disturbance wavelength is $\Lambda_{NS} = 0.088\,m$ ($\Lambda_{LSA} = 0.090\,m$) and growth rate is $-Im[\alpha_{NS}] = 0.070\,m^{-1}$ ($-Im[\alpha_{LSA}] = 0.064\,m^{-1}$).

Figure 5 shows the streamwise evolution of the vorticity field at a fixed time when the inlet condition is subject to low amplitude forcing with a frequency of $\omega = 0.33$. Subtracting the time-averaged solution from the full transient solution itself, we obtain the disturbance profiles which are then used to calculate the disturbance wavelength and growth rate. Good agreement with linear stability analysis' results is achieved.

### 3.3 Three-Dimensional Flows

The final test case considered in the present paper is known as the axisymmetric free jet. This three-dimensional flow is formed when a stream of speed $U_j$ issues from a pipe or nozzle into quiescent surroundings. The maximum jet streamwise velocity occurs at the center axis of the round pipe/nozzle, which has a diameter $D_0 = 2\,R_0$. We do not consider the injection pipe/nozzle in our simulations. The inlet, and also initial, condition for the velocity field at the initiation of the shear layer was the hyperbolic tangent profile for the streamwise component and zero for the other components. Such a profile is commonly used in linear stability analysis (Michalke and Hermann, 1982; Jendoubi and Strykowski, 1994) and numerical simulations (Danaila and Boersma, 2000; Hilgers and Boersma, 2001) of free jets.

All variables but pressure, which was extrapolated, were specified at the inlet boundary. This way, we effectively imposed a no-slip condition at the inlet wall everywhere except close to the jet exit. In order to allow proper entrainment across the side boundaries, a simple variation of the well-known stress free boundary conditions (Boersma et al., 1998) was used, where the stress gradient normal to the boundary wall was considered zero. Simple tests have shown that this boundary condition works better, especially close to the inlet solid wall. The pressure was fixed at its atmospheric value at these boundaries. At first, this same boundary condition was used at the outflow boundary. However, the actual governing equations for the velocity field were used, but with the implicit viscous flux normal to the outflow boundary neglected, were used instead. This parabolized boundary condition improved significantly the results. In either case, pressure was fixed at its atmospheric value at this outflow boundary as well.

The planar mixing layer results reported previously were obtained on a uniform Cartesian grid. In order to have a proper resolution of the flow field without significantly increasing the computing time for each simulation, a non-uniform Cartesian grid was used in the three-dimensional simulations. This enabled us to refine the grid around the circular jet axis and stretch it so that the side boundaries were further way. The grid was refined once again within the last three grid points close to each computational boundary in order to increase numerical stability (Zhong and Tatineni, 2003). A uniform grid was used in the spanwise direction from $y = z = 0$ to $y = z \simeq 1.5\,R_0$, with $\Delta y = \Delta z \simeq 0.065\,R_0$, and stretched exponentially towards the side boundaries at $y = z \simeq 6\,R_0$, with a maximum spacing of $\Delta y = \Delta z \simeq 0.26\,R_0$. A uniform grid spacing was used in the streamwise direction from $x = 0$ to $x \simeq 6\,R_0$, with $\Delta x = 0.11\,R_0$. The number of grid points used was $N_x = 56$ and $N_y = N_z = 112$ in the streamwise and both spanwise directions. Initial studies involved simulating three different Reynolds numbers ($Re = U_j D_0/\nu = 500$, 750 and 1000) and three different inlet momentum thicknesses ($R_0/\theta_0 = 14$, 20 and 26), in a total of nine different case studies. We note that, under these conditions, a laminar free jet is obtained in the near-field. All other parameters were chosen to match the experimental apparatus used at the UCLA Combustion Research Laboratory (Megerian et al., 2007).

The influence of the modified stress free and parabolized outflow boundary conditions on the numerical solutions was quantified by varying the computational domain size. Figure 6 shows the radial velocity inside the shear-layer at different distances downstream of the jet exit and its variation with respect to physical time for both shorter and longer domains with $Re = 750$ and $R_0/\theta_0 = 20$. This velocity component was chosen because its mean value is close to zero and, hence, it represents the behavior of the velocity disturbance. It is important to note that the number of grid points used in the longer domain simulations was changed in all directions in order to maintain the same spatial accuracy used for the shorter domain. Two major conclusions can be drawn. First, a comparison between both plots in this figure shows that the solution starts to be altered by the outflow boundary approximately downstream of $x/R_0 \simeq 5$. This valid domain size is enough for the present study since it focusses on the free jet near-field only. Second, a steady-state is achieved because no random disturbances are introduced at the jet exit and the numerical error is not high enough to sustain the open shear-flow instability. Nevertheless, a high amplitude disturbance is introduced initially due to the fact that the inlet and initial conditions are not solutions of the governing equations. One can observe that the amplitude of these initial disturbance waves grow as they propagate downstream, as one would expect for a convectively unstable flow.

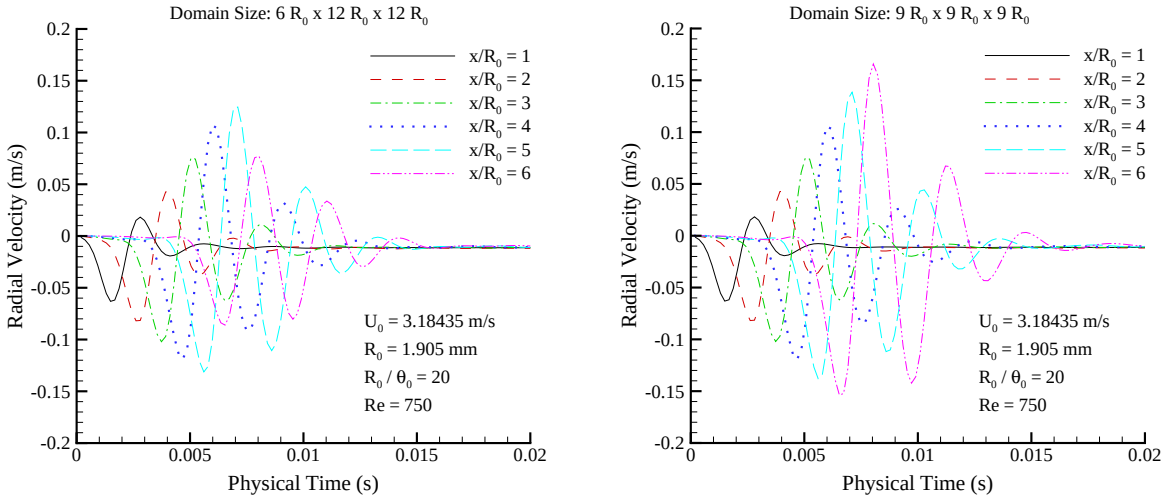


Figure 6. Shear-layer radial velocity behavior in physical time at different downstream locations for $Re = 750$ and $R_0/\theta_0 = 20$. (left) Shorter domain and (right) longer domain.

The steady-state streamwise velocity profile at different distances downstream of the jet exit is shown in Figure 7 (left) for $Re = 1000$ and $R_0/\theta_0 = 20$. The inlet profile is also shown for comparison. It should be noticed that these profiles are axisymmetric. The small under/over shooting observed in this solution disappears for the case with $Re = 500$ and $R_0/\theta_0 = 14$. Hence, the cause for this behavior is the inability of central difference schemes with artificial dissipation to properly resolve steep gradients. Nevertheless, one is able to observe in this figure that viscous dissipation smoothes these gradients as the flow propagates downstream of the jet exit, minimizing this problem.

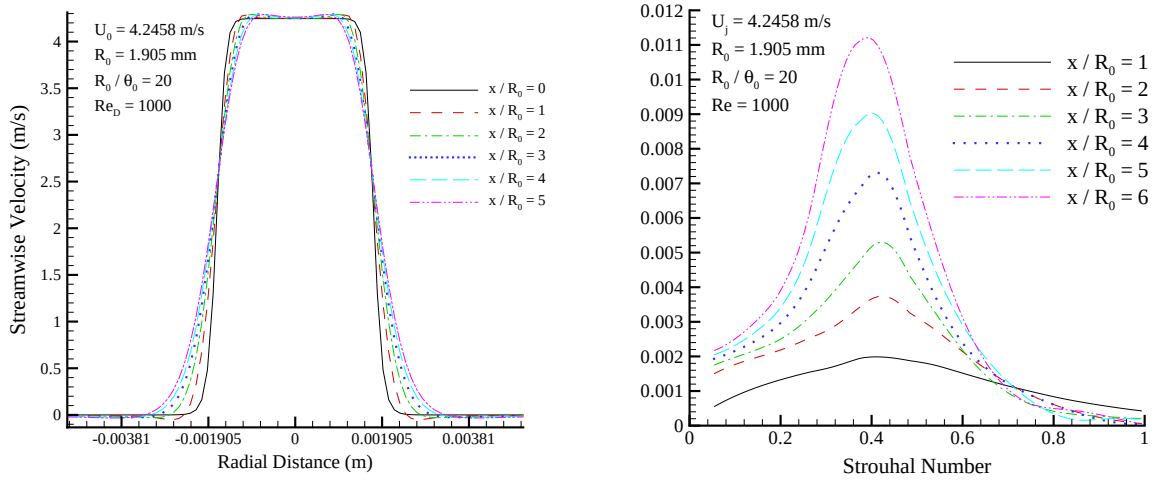


Figure 7. Profiles at different downstream locations for $Re = 1000$ and $R_0/\theta_0 = 20$: (left) Steady-state streamwise velocity component (right) Power spectra associated with radial velocity component.

Despite the fact that a steady-state is achieved, it is still possible to perform a Fourier transform of the transient radial velocity data associated with Figure 7 (left) at each downstream location. Such power spectra data reveals the natural Strouhal number of the flow, which is the frequency of the most amplified disturbance. These results are shown in Figure 7 (right), with a variation in the natural Strouhal number between $St = f^* D_0/U_j = 0.391$ and $0.411$, with the highest value measured at $x/R_0 = 1$ and the lowest at $x/R_0 = 6$. This decrease is expected since the Strouhal number is known to decrease as the momentum thickness increases (Ho and Huerre, 1984; Huerre and Monkewitz, 1990). Furthermore, this value of Strouhal number is within the range reported in the literature $0.3 < St < 0.6$ (Crow and Champagne, 1971; Michalke, 1984; Ho and Huerre, 1984).

We now perform a low amplitude forcing of the axisymmetric disturbance mode as a final test for the three-dimensional free jet simulations. In order to do so, the jet exit profile is modified by letting

$$U_j = 1 + A_j \, \sin[2\,\pi \, St_f \, t] \; , \tag{13}$$

where $St_f$ is the forcing Strouhal number and $A_j$ is the disturbance amplitude. The forcing parameters are $St_f = 0.4$ and $A_j = 0.02$, and the free jet exit parameters are $Re = 500$ and $R_0/\theta_0 = 20$. The forcing frequency $St_f$ lies approximately in the middle of the range of computed natural frequencies for the free jet shown previously. The domain size was increased to $10\,D_0$ in the streamwise direction and to about $7.5\,D_0$ in both spanwise directions.

Figure 8 (left) shows the power spectrum taken at different locations downstream of the jet exit, in the middle of the shear-layer. As expected, the forcing frequency $St_f$ is the dominant frequency. Furthermore, we see the amplitude of the disturbance being forced beginning to saturate between 4 and 5 radii downstream. This coincides with the increase in amplitude of the first subharmonic of the forcing frequency, as is also expected (Ho and Huerre, 1984). Higher harmonics are also present but with low amplitude, indicating the presence of weak nonlinear effects in the free jet near-fielld.

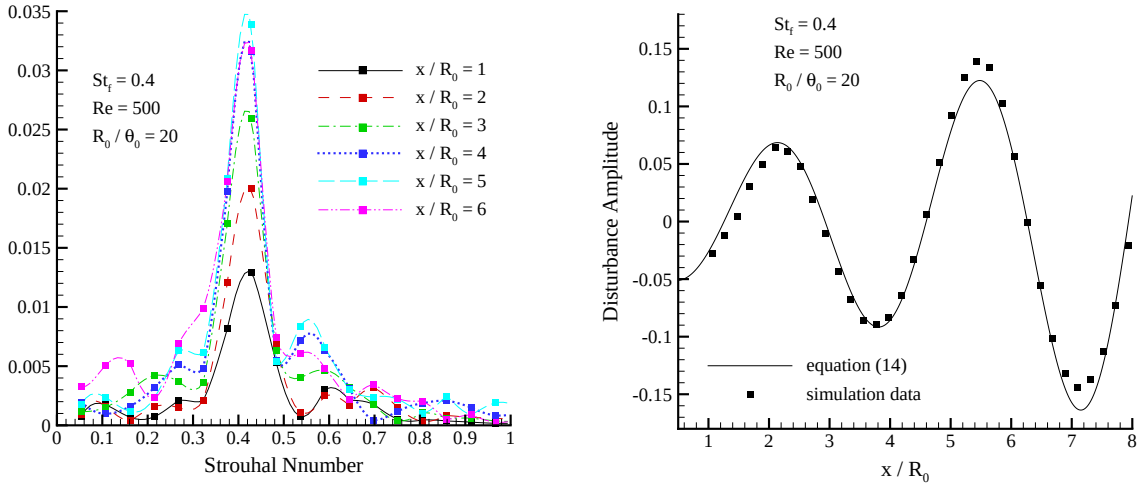


Figure 8. Low amplitude forcing with $St_f = 0.4$, $Re = 500$ and $R_0/\theta_0 = 20$: (left) Power spectra at different downstream locations (right) Disturbance spatial growth at dimensionless physical-time $t = t^* D_0/U_j = 14.75$.

In order to further validate this simulation, we estimate the wavenumber and growth rate of the linear disturbances in the near field of the jet exit. For that we use the function

$$A \sim A_{NS} \;\; \exp[Im[\alpha_{NS}] \;\; x] \, \cos[\phi_{NS} - Re[\alpha_{NS}] \;\; x] \;\; , \tag{14}$$

to fit the disturbance data extracted from the numerical simulation using the function **NonLinearRegress** from the software *Mathematica* (Wolfram, 1999). This function uses a nonlinear least-square fit coupled with a number of regression diagnostics to find the best values for the initial amplitude $A_0$, growth rate and wavenumber $\alpha_{NS}$, and phase $\phi_{NS}$. A comparison is shown in Figure 8 (right). We find the wavenumber to be $Re[\alpha_{NS}] \simeq 1.85$ and the growth rate to be $-Im[\alpha_{NS}] \simeq 0.19$. On the other hand, the inviscid local linear stability analysis of the hyperbolic tangent profile that models the free jet yields $Re[\alpha_{LSA}] \simeq 1.76$ for the wavenumber and $-Im[\alpha_{LSA}] \simeq 0.88$ for the growth rate. Similarly to the planar mixing layer analysis, the linear stability and numerical simulation wavenumbers agree reasonably well and a bigger disparity is seen for the respective growth rates. However, the higher value of the inviscid stability's growth rate in the free jet analysis is expected due to the low Reynolds number used in the numerical simulation (Morris, 1976).

## 4. CONCLUSIONS

The approximate factorization error arising from the use of an ADI method in pseudo-time slows down convergence after a few orders of magnitude. Recent research has show that the use of a successive over-relaxation by lines method instead significatively improves convergence. Furthermore, the use of central-differencing with artificial dissipation for spatial derivatives is troublesome for high Reynolds number flows. This code is currently being improved to include preconditioned upwind schemes with TVD capabilities. Nevertheless, this methodology was able to accurately solve incompressible flows at very low Mach numbers. Future research includes validation studies for flows with severe temperature gradients for incompressible, subsonic and transonic flows.

## 5. ACKNOWLEDGEMENTS

The authors would like to acknowledge the financial support of CAPES/Brazil, the UCLA Graduate Division, the National Science Foundation under Grants CTS-0200999 and CTS-0457413 and NASA under Grant NCC-157.

## 6. REFERENCES

Alves, L.S. de B., 2006, "Transverse Jet Shear-Layer Instabilities: Linear Stability Analysis and Numerical Simulations", Ph.D. Thesis, University of California at Los Angeles, USA.

Boersma, B.J., Brethouwer, G., Nieuwstadt, F.T.M., 1998, "A Numerical Investigation on the Effect of the Inflow Conditions on the Self-Similar Region of a Round Jet", Physics of Fluids, Vol. 10, No. 4, pp. 899-909.

Buelow, P.E.O., Venkateswaran, S., Merkle, C.L, 2001, "Stability and Convergence Analysis of Implicit Upwind Schemes", Computers and Fluids, Vol. 30, pp. 961-988.

Choi, Y.H., Merkle, C.L., 1993, "The Application of Preconditioning in Viscous Flows", Journal of Computational Physics, Vol. 105, pp. 207-223.

Danaila, I., Boersma, P.J., 2000, "D.N.S. of Bifurcating Jets", Physics of Fluids, Vol. 12, No. 5, pp. 1255-1257.

Guillard, H., Viozat, C., 1999, "On the Behavior of Upwind Schemes in the Low Mach Number Limit", Computers and Fluids, Vol. 28, pp. 63-86.

Hilgers, A., Boersma, B.J., 2001, "Optimization of Turbulent Jet Mixing", Fluid Dyn. Res., Vol. 29, pp. 345-368.

Ho, C.M., Huerre, P., 1984, "Perturbed Free Shear Layers", Annual Review of Fluid Mechanics, Vol. 16, pp. 365-424.

Huerre, P., Monkewitz, P.A., 1990, "Local and Global Instabilities in Spatially Developing Flows", Annual Review of Fluid Mechanics, Vol. 22, pp. 473-537.

Jendoubi, S., Strykowski, P.J., 1994, "Absolute and Convective Instability of Axisymmetric Jets with External Flow", Physics of Fluids, Vol. 6, No. 9, pp. 3000-3009.

Klainerman, S., Majda A., 1982, "Compressible and Incompressible Fluids", Communications on Pure and Applied Mathematics, Vol. 35, pp. 629-651.

Megerian, S., Davitian, J., Alves, L.S.B., Karagozian, A.R., 2007, "Transverse Jet Shear Layer Instabilities. Part I: Experimental Studies.", Journal of Fluid Mechanics, Vol. 593, pp. 93-129.

Merkle, C.L., Sullivan, J.Y., Buelow, P.E.O., Venkateswaran, S., 1998, "Computation of Flows with Arbitrary Equations of State", AIAA Journal, Vol. 36, No. 4, pp. 515-521.

Michalke, A., 1984, "Survey on Jet Instability Theory", Progress in Aerospace Science, Vol. 21, pp. 159-199.

Michalke, A., Hermann, G., 1982, "On the Inviscid Instability of a Circular Jet with External Flow", Journal of Fluid Mechanics, Vol. 114, pp. 343-359.

Morris, P.J., 1976, "The Spatial Viscous Instability of Axisymmetric Jets", J. of Fluid Mech., Vol. 77, pp. 511-529.

Sesterhenn, J., Muller, B., Thomann, H., 1999, "On the Cancelation Problem in Calculating Compressible Low Mach Number Flows", Journal of Computational Physics, Vol. 151, pp. 597-615.

Shuen, J.S., Chen, K.H., Choi, Y.H., 1993, "A Coupled Implicit Method for Chemical Non-Equilibrium Flows at All Speeds", Journal of Computational Physics, Vol. 106, pp. 306-318.

Tannehill, J.C., Anderson, D. A., Pletcher, R.H., 1997, "Computational Fluid Mechanics and Heat Transfer", Ed. Taylot & Francis, Philadelphia, USA.

Venkateswaran, S., Merkle, C.L, 2000, "Efficiency and Accuracy Issues in Contemporary CFD Algorithms", AIAA Technical Paper, No. 2000-2251.

Wilcox, D.C., 2000, "Basic Fluid Mechanics", Ed. DCW Industries, USA.

Wolfram, S., 1999, "The Mathematica Book", Ed. Wolfram Media, Cambridge, USA.

Zhong, X., Tatineni, M., 2003, "High-Order Non-Uniform Grid Schemes for Numerical Simulation of Hypersonic Boundary-Layer Stability and Transition", Journal of Computational Physics, Vol. 190, No. 2, pp. 419-458.

## 7. Responsibility notice

The author(s) is (are) the only responsible for the printed material included in this paper